

Simulated Diurnal Pulses in Hurricane Dorian (2019)

JEREMIAH O. PIERSANTE,^a KRISTEN L. CORBOSIERO,^a AND ROBERT G. FOVELL^a

^a *Department of Atmospheric and Environmental Sciences, University at Albany, State University of New York, Albany, New York*

(Manuscript received 7 March 2023, in final form 11 August 2023, accepted 14 August 2023)

ABSTRACT: Radially outward-propagating, diurnal pulses in tropical cyclones (TCs) are associated with TC intensity and structural changes. The pulses are observed to feature either cloud-top cooling or warming, so-called cooling pulses (CPs) or warming pulses (WPs), respectively, with CPs posing a greater risk for hazardous weather because they often assume characteristics of tropical squall lines. The current study evaluates the characteristics and origins of simulated CPs using various convection-permitting Weather Research and Forecasting (WRF) Model simulations of Hurricane Dorian (2019), which featured several CPs and WPs over the tropical Atlantic Ocean. CP evolution is tested against choice of microphysics parameterization, whereby the Thompson and Morrison schemes present distinct mechanisms for CP creation and propagation. Specifically, the Thompson CP is convectively coupled and propagates outward with a rainband within 100–300 km of the storm center. The Morrison CP is restricted to the cirrus canopy and propagates radially outward in the upper-level outflow layer, unassociated with any rainband, within 200–600 km of the storm center. The Thompson simulation better represents the observations of this particular event, but it is speculated that CPs in nature can resemble characteristics from either MP scheme. It is, therefore, necessary to evaluate pulses beyond just brightness temperature (e.g., reflectivity, rain rate), especially within simulations where full fields are available.

SIGNIFICANCE STATEMENT: Tropical cyclone size and structure are influenced by the time of day. Identifying and predicting such characteristics is critical for evaluating hazardous weather risk of storms close to land. While satellite observations are valuable for recognizing daily fluctuations of tropical cyclone clouds as seen from space, they do not reliably capture what occurs at the surface. To investigate the relationship between upper-level cloud oscillations and rainbands, this study analyzes simulations of a major hurricane along the coast of Florida. The results show that rainbands are not always tied to changes in cloud tops, suggesting multiple pathways toward the daily oscillation of upper-level tropical cyclone clouds.

KEYWORDS: Tropical cyclones; Cloud microphysics; Numerical analysis/modeling; Diurnal effects

1. Introduction

“Diurnal pulses” in the satellite infrared brightness temperature (IRBT) field surrounding a tropical cyclone (TC) are often associated with hazardous weather, and changes in TC intensity and structure (Dunion et al. 2014, 2019). A “cooling pulse” (CP), one type of diurnal pulse, is the outward propagation of an IRBT cooling trend that forms a quasi-symmetric ring around the TC center. The CP is typically constrained to the inner core overnight. Upon sunrise, the CP propagates radially outward from the TC inner core at approximately $5\text{--}10\text{ m s}^{-1}$ such that it reaches 500 km in radius by sunset. CPs that follow this diurnal schedule are termed “on-the-clock” (see Dunion et al. 2014, Fig. 10), occurring on 72% of 1982–2017 Atlantic TC days (Ditchek et al. 2019b). Warming pulses (WPs), the other type of diurnal pulse, are the outward propagation of IRBT warming, occurring on-the-clock on 16% of TC days. Thus, diurnal pulses, which are primarily CPs, are nearly ubiquitous among Atlantic basin TCs (Ditchek et al. 2019b).

CPs are more common among mature TCs, and in environments with less vertical wind shear and greater favorability for deep convection (e.g., enhanced sea surface temperatures, moisture, low-level vorticity, and upper-level divergence;

Dunion et al. 2014; Ditchek et al. 2019b; Knaff et al. 2019). In contrast, WPs are more common within higher shear environments, lower intensity storms, and environments less favorable for deep convection (Ditchek et al. 2019b). Most of the diurnal pulse discussion in recent literature has focused on CPs because they are much more likely to be associated with hazardous weather, as they can take on characteristics associated with tropical squall lines such as lightning, enhanced rain rates, and surface cold pools (Dunion et al. 2019; Ditchek et al. 2019a, 2020; Trabling and Bell 2021). At upper levels, they also feature increased hydrometeor mixing ratios, outflow, and upward vertical motion (Dunion et al. 2019; Ditchek et al. 2019a, 2020; Trabling and Bell 2021). Furthermore, approximately 50% of CPs worldwide between 2001 and 2018 were coupled with precipitation pulses (PPs), where a PP is the outward propagation of increased rain rate (Zhang and Xu 2022). Like CPs, PP frequency increases with TC intensity. An important distinction is that while CPs often propagate outward to 500 km, PPs generally weaken and fade around 300 km. Thus, Zhang and Xu (2022) argue that while CPs are associated with increased rain rates within inner radii, CPs decouple from deep convection and continue propagating only at upper levels at outer radii.

It is well established that the TC diurnal cycle (TCDC) is driven by shortwave- and longwave-radiation-induced instability (Ge et al. 2014; Melhauser and Zhang 2014; Tang and Zhang 2016; Navarro and Hakim 2016; Ruppert and O’Neill 2019;

Corresponding author: Jeremiah O. Piersante, jpiersante@albany.edu

Dunion et al. 2019; Lee et al. 2020; Zhang et al. 2020; Duran et al. 2021). The source of the instability results from a robust diurnal cycle of radiative heating and cooling of the upper-level TC outflow layer near 200 hPa (Ruppert and O'Neill 2019; Dunion et al. 2019), which is where diurnal pulses are detected from IRBT. The trigger mechanisms of CPs and WPs, however, and how they fit into the context of the TCDC, remain unclear, and complicated by the fact that many occur “off-the-clock” at atypical times during the day (Ditchek et al. 2020; Trabling and Bell 2021).

While several studies have used numerical weather prediction to identify characteristics of CPs and their environments (Dunion et al. 2019; Ruppert and O'Neill 2019; Ditchek et al. 2020), none have yet to invoke simulations to determine the source of pulses themselves. The current study utilizes simulations of major Hurricane Dorian (2019), in which various CPs and WPs occurred in nature, to investigate the following:

- 1) How does choice of microphysics (MP) scheme impact CP characteristics? How do simulated CPs compare to the observed?
- 2) What is the origin of CPs, and what causes their outward propagation?

Since IRBT fluctuations are functions of upper-level hydrometeors, and because hydrometeors are handled differently among MP parameterizations, it is hypothesized that questions 1 and 2 will largely differ for each MP scheme. We also suspect that the origin and propagation of CPs are related to their frequent convective-coupling nature (Ditchek et al. 2019a, 2020; Trabling and Bell 2021).

Section 2 details our experimental setup, which includes a numerical weather prediction model and several observational datasets. Section 3 describes characteristics of simulated and observed storms, and their corresponding diurnal pulses during the study time frame. Origins of simulated CPs are also identified and discussed. Last, section 4 summarizes our conclusions within the context of previous work.

2. Methodology

a. Model setup

The Advanced Research Weather Research and Forecasting (WRF) Model version 4.3.1 (Skamarock et al. 2019) was used to conduct two simulations of Hurricane Dorian (2019) to compare diurnal pulses. The model had outer (D01; 361×321) and inner (D02; 841×721) domains of 12- and 3-km horizontal grid spacing, respectively (Fig. 1), and 57 vertical levels (50-hPa top). Both simulations were initialized and forced with 3-h, 0.5° Global Forecast System (GFS) forecasts, obtained from the National Centers for Environmental Information (NCEI) database.¹ The GFS was chosen for initial and boundary conditions because it has global coverage and is commonly used to initialize forecast models directly or indirectly (e.g., in the North American Mesoscale Forecast System and High-Resolution

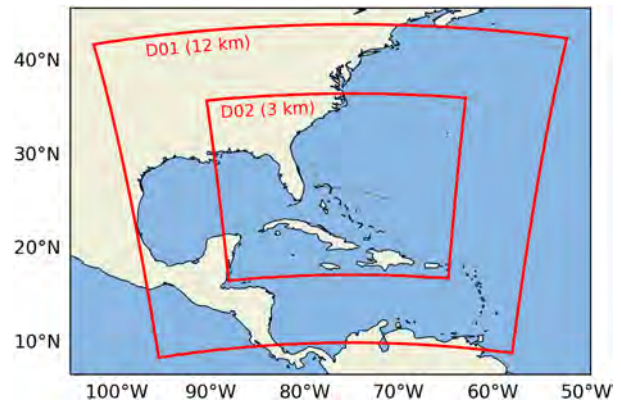


FIG. 1. WRF outer (D01) and inner (D02) domains. The observed Hurricane Dorian (2019) track for 0000 UTC 31 Aug–1200 UTC 4 Sep, derived from HURDAT2, is shown in gray dashes for reference.

Rapid Refresh). Physical parameterizations included the MYNN 2.5 planetary boundary layer scheme (Nakanishi and Niino 2009), RRTMG shortwave and longwave radiation schemes (Iacono et al. 2008), Noah surface physics (Niu et al. 2011), and Kain-Fritsch cumulus scheme (D01 only; Kain 2004).

For MP scheme, simulations used either Thompson (Thompson et al. 2008) or Morrison (Morrison et al. 2009). Both realistic runs, termed Thompson CTRL and Morrison CTRL, respectively, were initialized with a cold start at 0000 UTC 31 August 2019 and run for 4.5 days. Thompson and Morrison are popular MP parameterizations with important distinctions. Since Thompson more rapidly transitions cloud ice to snow in the model, Morrison tends to have greater quantities of free-floating cloud ice in the upper troposphere (Bao et al. 2019), which will impact how diurnal pulses are portrayed.

b. Model output and observation analysis

TC characteristics (e.g., intensity, size, structure) were compared among simulations in addition to the observations. The HURDAT2 “best track” (Landsea and Franklin 2013) provided Dorian’s observed center location, minimum sea level pressure (MSLP), and maximum sustained surface (10-m) wind speed at 6-h intervals. For the simulated TCs, a pressure centroid algorithm based on Eq. (2) from Nguyen et al. (2014) was used to determine TC centers, where MSLP is used as a first guess, then the center is adjusted using the 2D simulated surface pressure gradient field:

$$\bar{x} = \frac{\sum_{r=0}^R x_i P'_i}{\sum_{r=0}^R P'_i}, \quad \bar{y} = \frac{\sum_{r=0}^R y_i P'_i}{\sum_{r=0}^R P'_i}, \quad (1)$$

where \bar{x} and \bar{y} are the longitude and latitude, respectively; R is the outer radius of the inner core; x_i and y_i are points within the inner core; and P'_i is the environmental pressure (1013 hPa) minus each point’s pressure. The result is a smoother and more accurate TC track relative to simply using minimum MSLP

¹ <https://www.ncei.noaa.gov/products/weather-climate-models/global-forecast>.

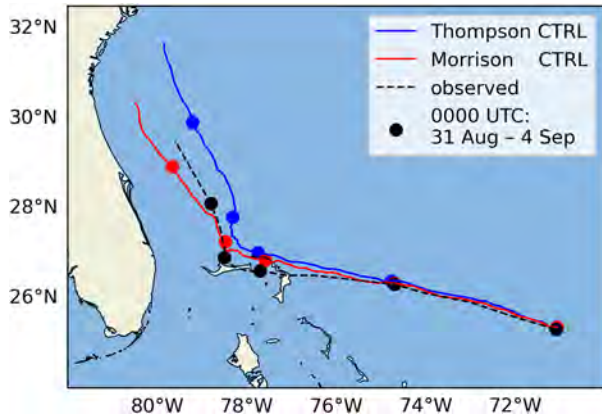


FIG. 2. Simulated and observed TC tracks in D02. Thompson CTRL and Morrison CTRL tracks are blue and red, respectively. The observed Hurricane Dorian (2019) track, derived from HURDAT2, is shown in black dashes. Dots along each track denote 0000 UTC on each day of the simulation period: 0000 UTC 31 Aug–1200 UTC 4 Sep.

locations. Storm-centered variables are calculated with respect to these locations throughout the TC simulations.

GridSat-B1 (Knapp et al. 2011) provided 3-h global measurements of observed IRBT at 11 μm , which were used to examine the size and pulsing of Dorian’s cirrus canopy. Simulated IRBT was calculated with respect to the top of atmosphere outgoing longwave radiation (OLR) WRF output variable:

$$\text{IRBT} = \sqrt[4]{\frac{\text{OLR}}{\sigma}}, \quad (2)$$

where σ is the Stefan–Boltzmann constant, $5.6704 \times 10^{-8} \text{ W m}^{-2} \text{ K}^{-4}$ (Petty 2006). Simulated and observed CPs and WPs were subjectively identified using storm-centered plan maps and Hovmöller diagrams of axisymmetric 6-h IRBT differences. Previous studies also use these 6-h backward differences in IRBT to identify pulses, where $\Delta\text{IRBT}(t) = \text{IRBT}(t) - \text{IRBT}(t - 6)$ (Dunjon et al. 2014; Ditchek et al. 2019a,b, 2020). Here, an outward propagation of cooler or warmer IRBT for at least 200 km at a phase speed approximately $5\text{--}10 \text{ m s}^{-1}$ was considered a CP or a WP, respectively. The following results will primarily discuss a CP that occurred on 1 September within both simulated storms. It will be shown that despite a similar onset time, the simulated CPs largely differed in terms of their structure and direct/indirect impacts.

3. Characteristics of Dorian pulses

a. Track and intensity of simulated and observed storms

The simulated CTRL and observed storms tracked westward toward Florida for the first 2 days of the simulation period (Fig. 2). Upon crossing the northernmost Bahamas Islands by 2 September, all three storms recurved toward the northwest. Thompson CTRL recurved first and was farthest

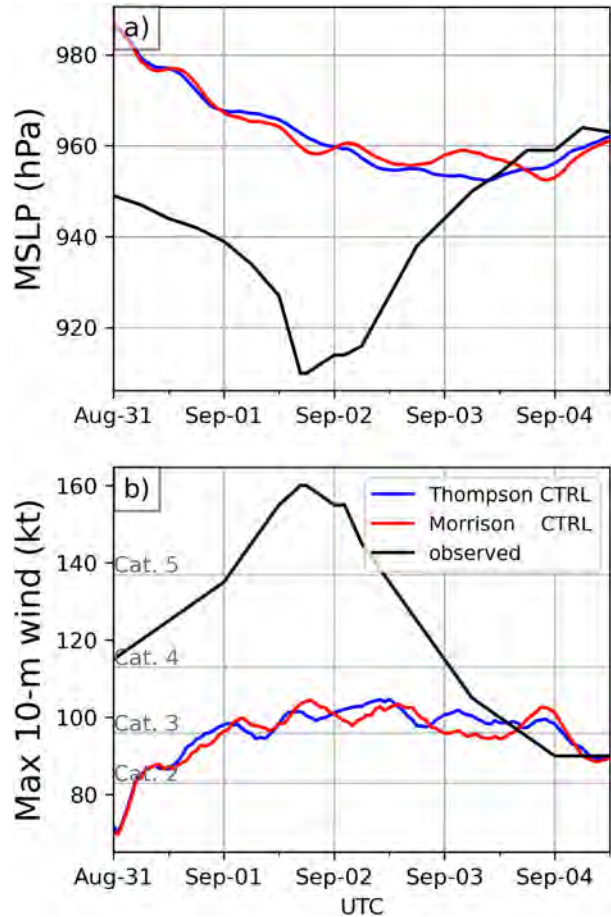


FIG. 3. (a) MSLP (hPa) and (b) maximum sustained 10-m wind speed (kt; $1 \text{ kt} = 0.51 \text{ m s}^{-1}$) for Thompson CTRL (blue), Morrison CTRL (red), and the observed (black) storms.

east for the last 2 days of the simulation, while Morrison CTRL was the westmost. TC simulations with different MP schemes have been known to produce diverging tracks owing to the different quantities of hydrometeor species, which impacts the cloud–radiative forcing and, thus, the TC structure and steering (Fovell et al. 2010; Bu et al. 2014). The observed storm was farthest south until 3 September, then after recurvature was positioned between the simulations while moving the slowest. See Hazelton et al. (2023) for a thorough investigation of the factors that influenced Hurricane Dorian’s track.

While there were only subtle differences in simulated MSLP and 10-m wind speed between the Thompson and Morrison CTRLs, the observed storm was much more intense than both CTRLs (Fig. 3). The intensity discrepancy occurred immediately, likely owing to the coarse initial GFS resolution of 0.5° . The observed storm continued to intensify to category 5 as the models spun up, which could partially explain why simulated intensities never reached the observed. We acknowledge that the differences between the simulations and observations are nonnegligible; however, the scope of the current study is diurnal pulses, which were featured in all storms. Specifically, on 1 September, a CP occurred in the

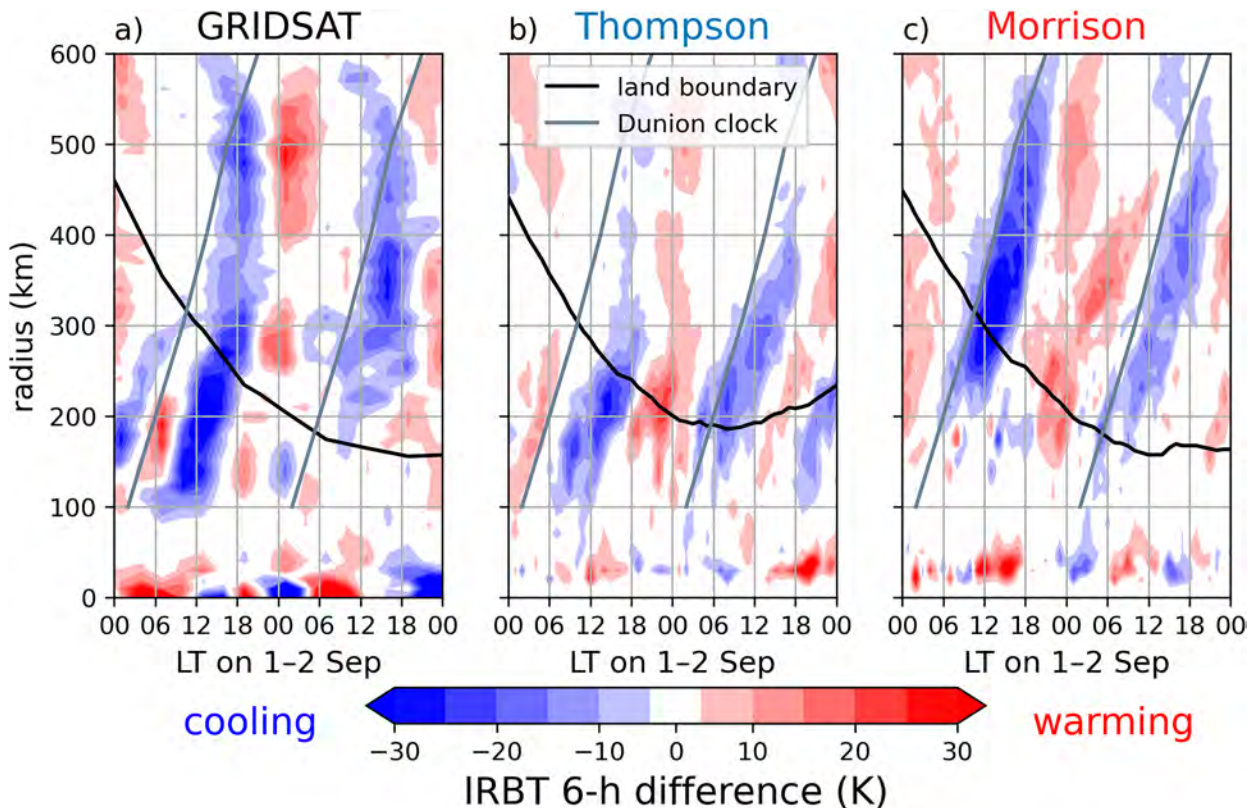


FIG. 4. Hovmöller diagrams of storm-centered IRBT 6-h differences (K; shaded) on 1–2 Sep LT for (a) observed (GridSat), (b) Thompson CTRL, and (c) Morrison CTRL. The IRBT fields are azimuthally averaged about the western side of each storm to maximize the signal of pulses, where $\Delta\text{IRBT}(t) = \text{IRBT}(t) - \text{IRBT}(t - 6)$. Blue and red shading indicate IRBT cooling and warming, respectively, so each CP is represented as a coherent, propagating spread of blue. Diagonal gray lines indicate the typical LT (UTC - 5 h herein) and radius for an on-the-clock pulse (Dunjon et al. 2014). The storms are at least partially over land above the solid black curve.

observations, and both Thompson and Morrison CTRLs, which is discussed next.

b. Overview of simulated and observed pulses

The observed and two CTRL storms featured a variety of diurnal pulses during the period of interest, but we focus on 1 September when a CP occurred in the observed and simulated storms. As in previous studies (Dunjon et al. 2014; Ditchek et al. 2019a,b, 2020), Hovmöller diagrams of IRBT 6-h backward differences are used to identify pulses with respect to local time (LT; Fig. 4).² Herein, based on Dorian's longitude over this time period, LT = UTC - 5 h, corresponding to eastern standard time. The 1 September CPs commenced around 0600 LT (1100 UTC), giving the models over 30 h of spinup prior to analysis of simulated fields. After the 1 September CP, the simulations featured subsequent WPs and CPs, which ended on 2 September. Note that the Hovmöller diagrams in Fig. 4 are azimuthal averages of only the western side of the TC because this is where the pulses largely occurred (cf. Fig. 5). We explore the 1 September

CP because it was more pronounced in the simulations and observations, and spent less time over land compared to the 2 September CP.

CPs within the observations, Thompson CTRL, and Morrison CTRL first appeared at different radii. The observed and Thompson CTRL CPs were visible within the 100–300-km range, while Morrison CTRLs existed within 200–600 km, largely over land (above the black curve in Fig. 4c). As a result of their timing and radial position, the Morrison CTRL CP was nearly on-the-clock (gray diagonal line in Fig. 4), whereas the others were approximately 6 h off-the-clock. Note that the observed GridSat cooling on 1 September that occurred around 1800 LT between 300 and 600 km is not part of the CP because it was not propagating outward with time (Fig. 4a). Instead, land-based deep convection apart from any pulsing likely reduced IRBT, as suggested by radar imagery at this time (not shown). Thompson CTRL had a similar, albeit weaker, IRBT signature (Fig. 4b). Thus, each of the Thompson and GridSat CPs only occurred within 100–300 km.

The three 1 September CPs were clearest around 1300 LT west of the TC center; the Morrison CTRL was positioned at about 300 km, and those of Thompson CTRL and the observed were just within 200 km (Figs. 5b,d,f). The larger and more radially extensive CP of Morrison was likely a function

² Herein, blue represents IRBT cooling (i.e., CPs); red represents IRBT warming (i.e., WPs).

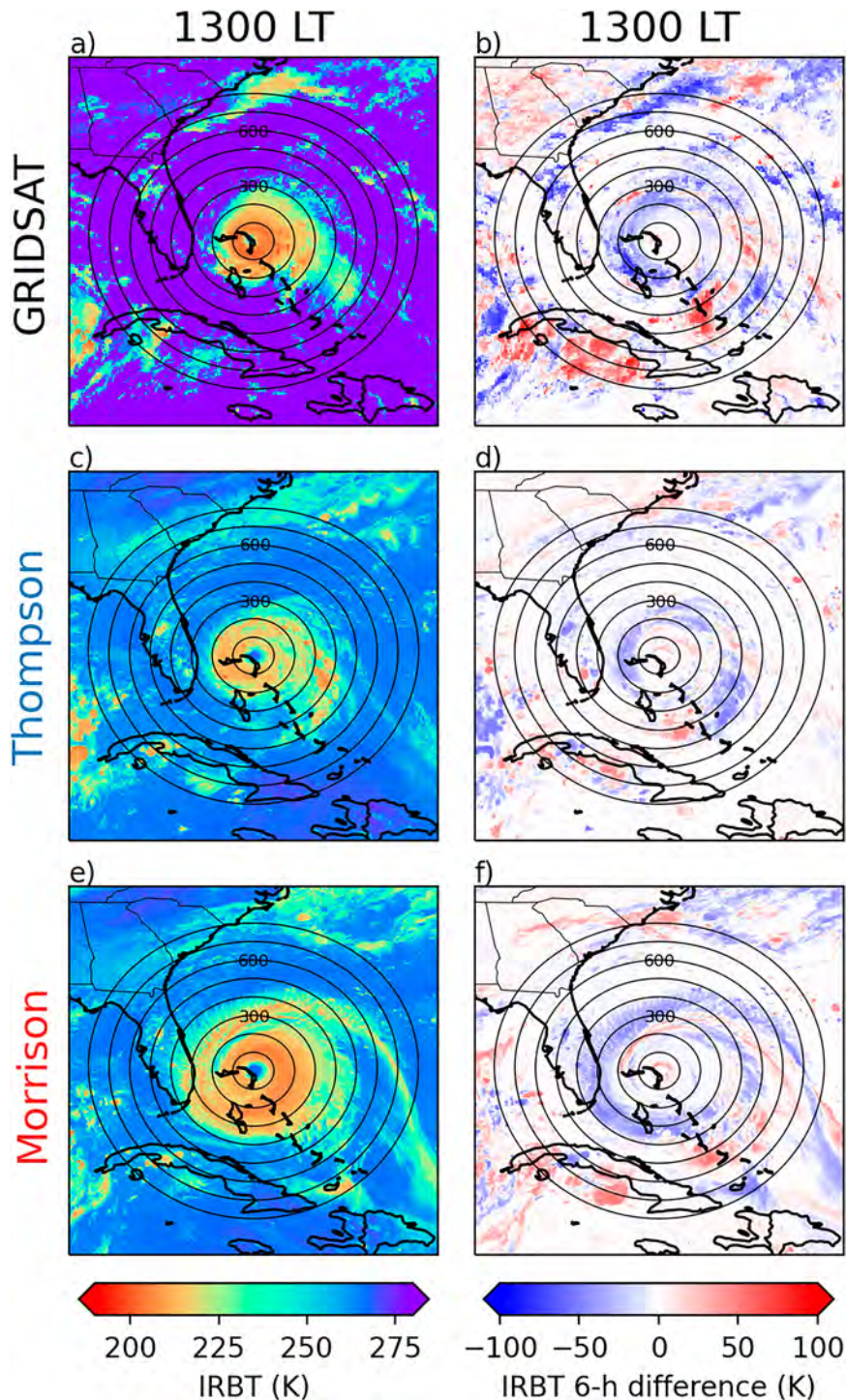


FIG. 5. Storm-centered plan maps of (a),(c),(e) IRBT (K) and (b),(d),(f) IRBT 6-h difference (K) at 1300 LT 1 Sep for (a),(b) the observed/GridSat; (c),(d) Thompson CTRL; and (e),(f) Morrison CTRL. Black rings about the storm center are every 100 km.

of a larger cirrus canopy, which extended outward to about 400 km (Fig. 5e). For reference, Thompson CTRL and the observed canopies reached only about 300 km in areal extent (Figs. 5a,c). Recall that a key difference between Morrison

and Thompson MP schemes is that the former leaves higher amounts of free-floating cloud ice in the upper troposphere, which leads to a more optically thick and expansive cloud shield, as notable through cooler IRBTs. Thus, it can be

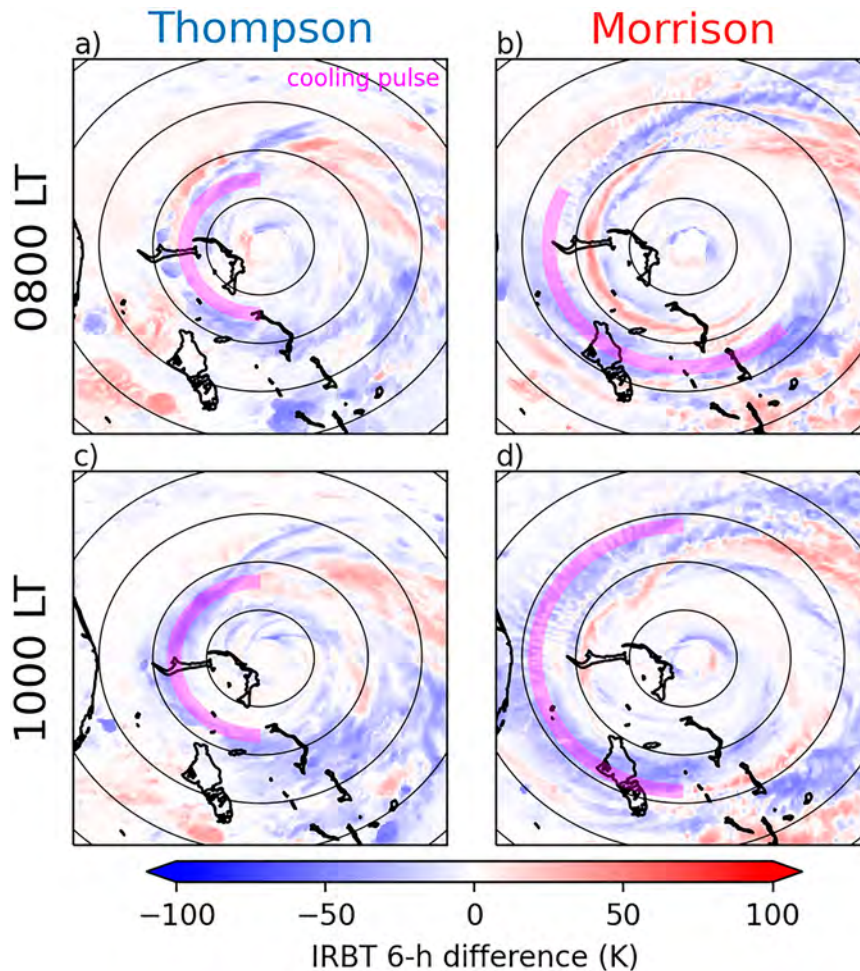


FIG. 6. Storm-centered plan maps of IRBT 6-h difference (K) for (a),(c) Thompson CTRL and (b),(d) Morrison CTRL at (a),(b) 0800 and (c),(d) 1000 LT 1 Sep. Approximate positions of the CP at each time step are marked by magenta shading. Black rings about the storm center are every 100 km.

inferred that greater amounts of upper-tropospheric cloud ice impacts CP size and magnitude, and how it is seen from space. The impact of different distributions of cloud ice between Thompson and Morrison CTRL is shown and discussed in the next section (cf. Fig. 12). Last, the Thompson CTRL cloud shield and CP better resembled the observations.

c. 1 September cooling pulse evolution and origin

1) HORIZONTAL CHARACTERISTICS OF COOLING PULSE PROPAGATION

Though Fig. 4 suggests that the CPs commenced near 0600 LT, the CPs are less obvious on plan maps at this time. Thus, the plan map evolution of the 1 September CTRL CPs is presented in Figs. 6 and 7 with 6-h IRBT difference snapshots at 0800, 1000, 1200, 1400, and 1600 LT. In Fig. 6, which shows out to ~ 350 km from each storm center at 0800 and 1000 LT, the two CPs were first identifiable in the 6-h IRBT field: the Thompson CTRL CP began

propagating just beyond 100 km and the Morrison CTRL CP just beyond 200 km, both most pronounced west of the TC centers.

At 1200 LT, the Thompson and Morrison CTRL CPs were 175 and 300 km west of the TC center, respectively (Figs. 7a,b). Both pulses propagated radially outward toward Florida as the storms slowly tracked westward. While the Morrison CTRL CP reached 400 km by 1600 LT (Fig. 7f), its Thompson counterpart reached only 225 km (Fig. 7e), indicating a much slower propagation speed. The Morrison CTRL CP propagation speed of approximately 6.9 m s^{-1} , calculated within 200–600 km, matches the climatological diurnal pulse propagation speed of $5\text{--}10 \text{ m s}^{-1}$ (Dunjon et al. 2014; Ditchek et al. 2019b). Thompson CTRL's CP speed of approximately 4.6 m s^{-1} , calculated within 100–300 km, is just short of that range. The observed CP's speed was approximately 5.6 m s^{-1} within 100–300 km, splitting the difference between the simulations' speeds.

To examine hazardous weather potential associated with the CPs, the evolution of composite reflectivity is assessed at

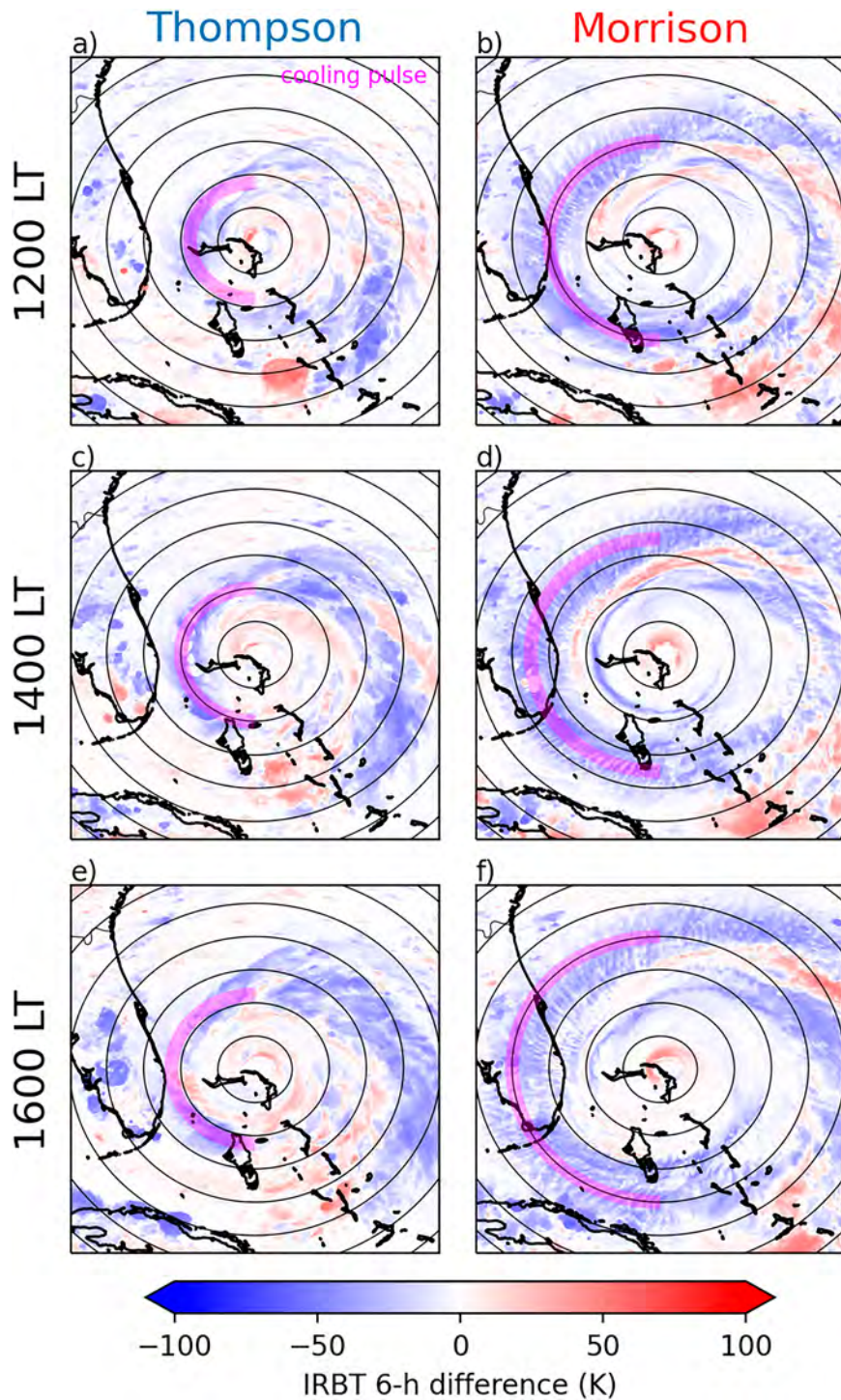


FIG. 7. Storm-centered plan maps of IRBT 6-h difference (K) for (a),(c),(e) Thompson CTRL and (b),(d),(f) Morrison CTRL at (a),(b) 1200; (c),(d) 1400; and (e),(f) 1600 LT 1 Sep. Positions of the CP at each time step west of the center are marked by magenta shading. Black rings about the storm center are every 100 km.

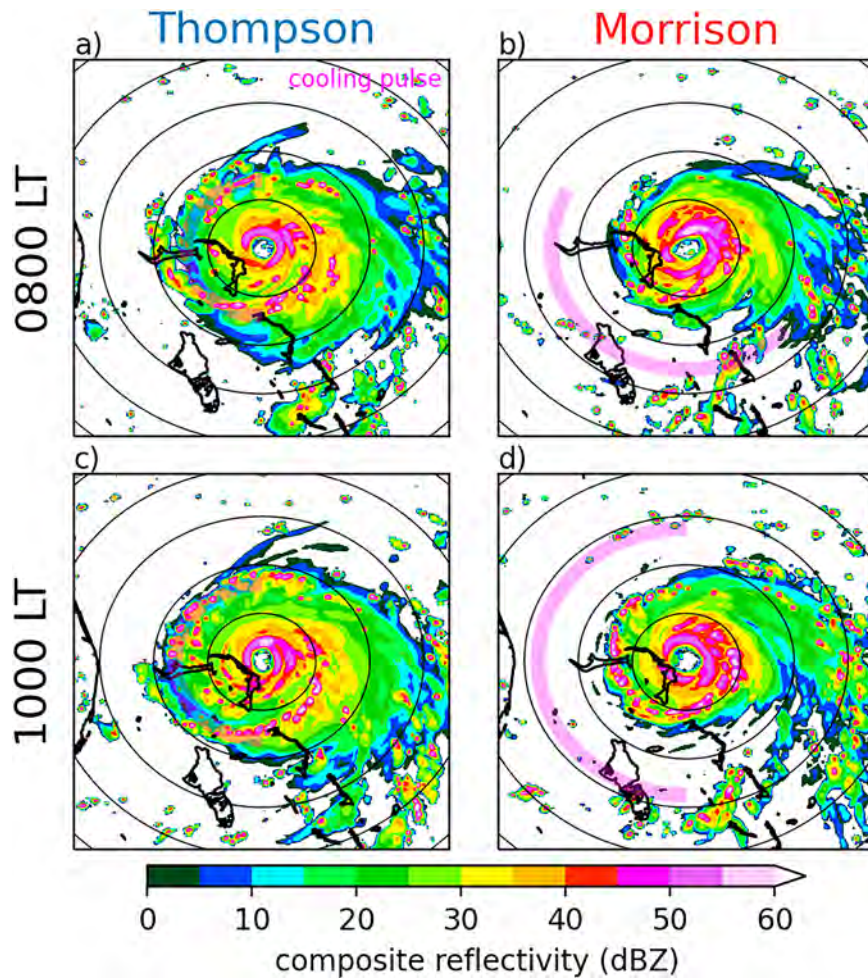


FIG. 8. As in Fig. 6, but for composite reflectivity (dBZ).

the same times as shown in Figs. 6 and 7 (Figs. 8 and 9). The more slowly propagating Thompson CTRL CP was associated with an outward propagating rainband throughout 0800–1600 LT (Figs. 8a,c and 9a,c,e), indicating the CP was convectively coupled. As shown by Ditchek et al. (2019a) and Zhang and Xu (2022), CPs associated with lightning and enhanced rain rates are common within 300 km of the TC center. Interestingly, the Morrison CTRL CP was not collocated with any convective or rainband feature, suggesting that the CP was restricted to the cirrus canopy. Note that Morrison CTRL included a rainband near 150 km early on like Thompson CTRL, just without IRBT cooling at the same radius (Figs. 8b,d).

Rain rates valid on 1–2 September also indicate that Thompson CTRL CPs were collocated with PPs (Fig. 10a). It should be noted that the two Thompson CTRL CPs were not identical, however. With the 1 September CP, the IRBT cooling propagated outward slightly faster than the associated increase in rain rate. On the other hand, the 2 September cooling and rain rate increase lined up well to 375 km (Fig. 10a). The WP between the two CPs was collocated with the decrease in rain rate, which seems to be a function of the 1 September rainband

leaving the area. As with composite reflectivity (Figs. 8 and 9), pulses within Morrison CTRL were not associated with any rain rate trend (Fig. 10b). The canopy-restricted nature of the Morrison CTRL CP and the convectively coupled nature of the Thompson CTRL CP from vertical perspectives are illustrated next (cf. Figs. 11 and 12).

2) VERTICAL CHARACTERISTICS AND ORIGINS OF COOLING PULSES

To further analyze the relationship between 6-h differences of IRBT and reflectivity, we construct their time series at fixed radii and calculate corresponding correlation coefficients (r) for 1 September (Fig. 11). Radii of interest are 200 and 300 km for Thompson and Morrison CTRLs, respectively, to target the locations where CPs featured the most rapid cooling rates in each simulation; recall that these two CPs occurred at slightly different radii (Figs. 4b,c). The IRBT cooling maximized just after 1200 LT in both Thompson and Morrison CTRLs at their respective radii. Upper-level reflectivity, calculated as the 10–15-km layer average, followed a similar trend, highlighting the increase in upper-level frozen hydrometeors associated with

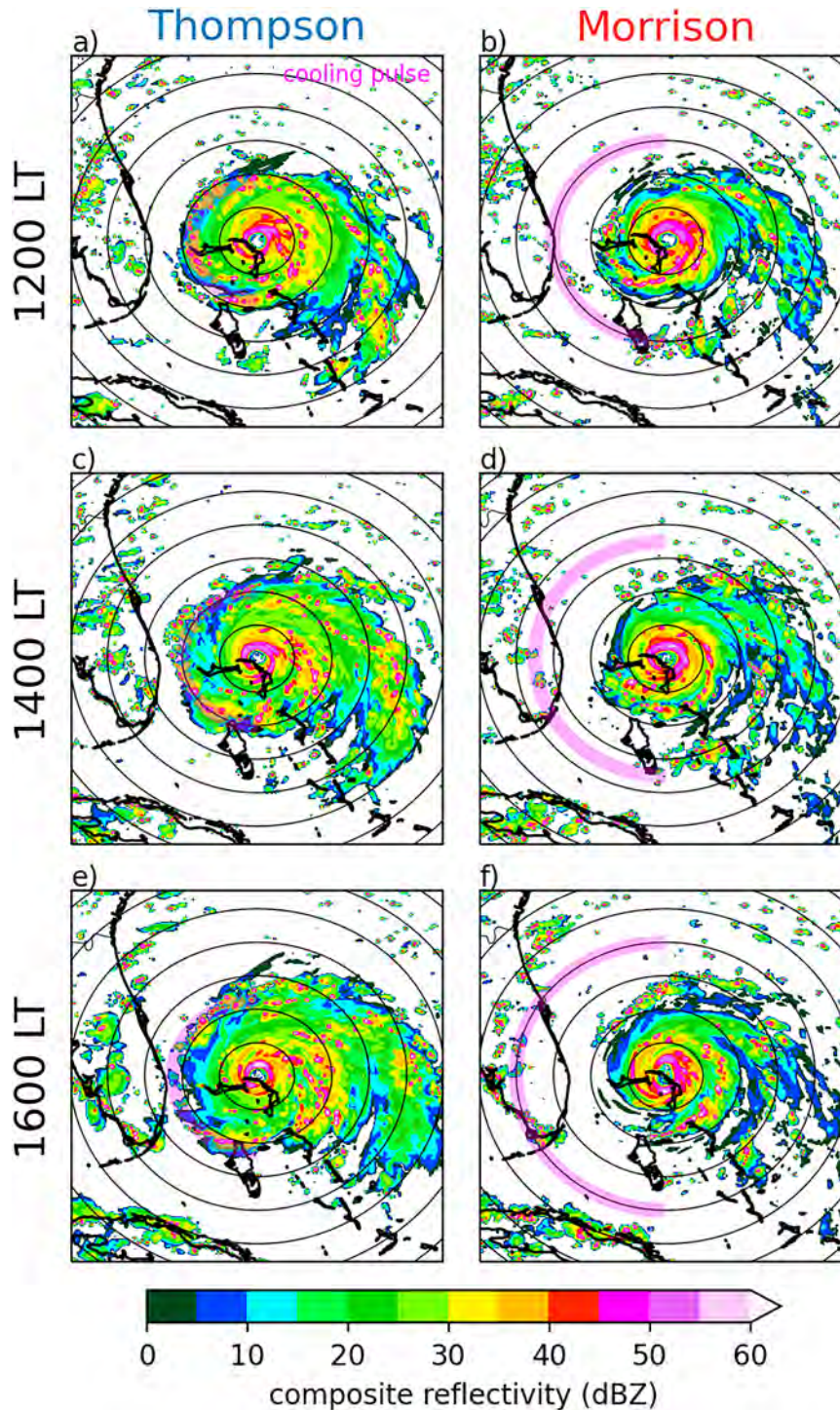


FIG. 9. As in Fig. 7, but for composite reflectivity (dBZ).

the decrease in IRBT. The r values calculated between 6-h upper-level reflectivity and IRBT on 1 September were -0.94 and -0.97 for Thompson and Morrison CTRLs, respectively, suggesting a robust, negative correlation between the two variables. Note that the 6-h IRBT difference axis is inverted to improve the

relationship visualization (Fig. 11); since a decrease in IRBT is associated with an increase in reflectivity, r values are negative.

A larger difference lies within the low-level reflectivity (0–5 km) and IRBT relationship, however: Thompson CTRL maintains a large r value of -0.89 , whereas that of

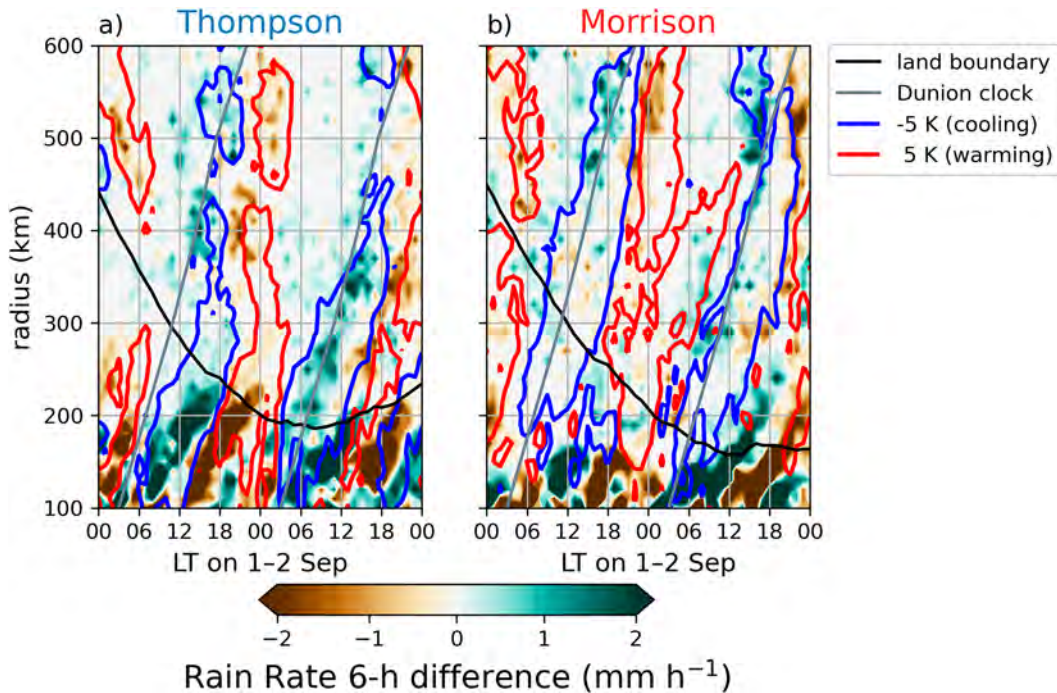


FIG. 10. Hovmöller diagrams of storm-centered rain rate 6-h differences (shaded; mm h^{-1}) and IRBT 6-h differences (blue and red contours; $\pm 5 \text{ K}$) on 1–2 Sep (hours in LT) for (a) Thompson CTRL and (b) Morrison CTRL. The IRBT and rain rate fields are azimuthally averaged about the western side of each storm to maximize the signal of pulses. Diagonal gray lines indicate the typical LT and radius for an on-the-clock pulse (Dunion et al. 2014). The storms are at least partially over land above the solid black curve. Fields within 100 km are omitted for aesthetic purposes because there were no detectable signals in that range.

Morrison CTRL drops to -0.67 . Again, the contrast in r values suggests the Thompson CTRL CP was associated with scatters in the lower troposphere (i.e., the rainband seen in Figs. 8a,c and 9a,c,e), while the Morrison CTRL CP was

restricted to the cirrus canopy. Interestingly, Morrison CTRL featured an increase in 0–5-km reflectivity at 300 km around 0900 LT (Fig. 11b). Because no rainband reached 300 km in Morrison CTRL (Figs. 8b,d and 9b,d,f), this 0–5-km reflectivity

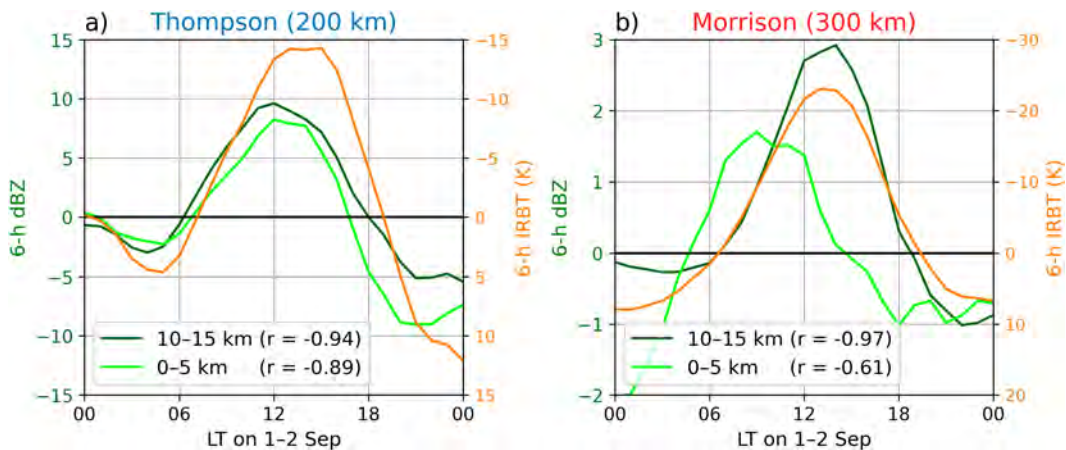


FIG. 11. IRBT (orange; K) and reflectivity (green; dBZ) 6-h differences at fixed radii on 1 Sep LT for (a) Thompson CTRL at 200 km and (b) Morrison CTRL at 300 km. Values are backward differences azimuthally averaged at the corresponding radial distance for the western half of the storm. Dark green and light green denote upper-level (10–15-km layer average) and lower-level (0–5-km layer average) reflectivity, respectively. Pearson correlation coefficients (r), calculated using `scipy.stats.linregress` (<https://docs.scipy.org/doc/scipy/reference/generated/scipy.stats.linregress.html>) between reflectivity layers and IRBT are shown. Note the differences in scales between (a) and (b).

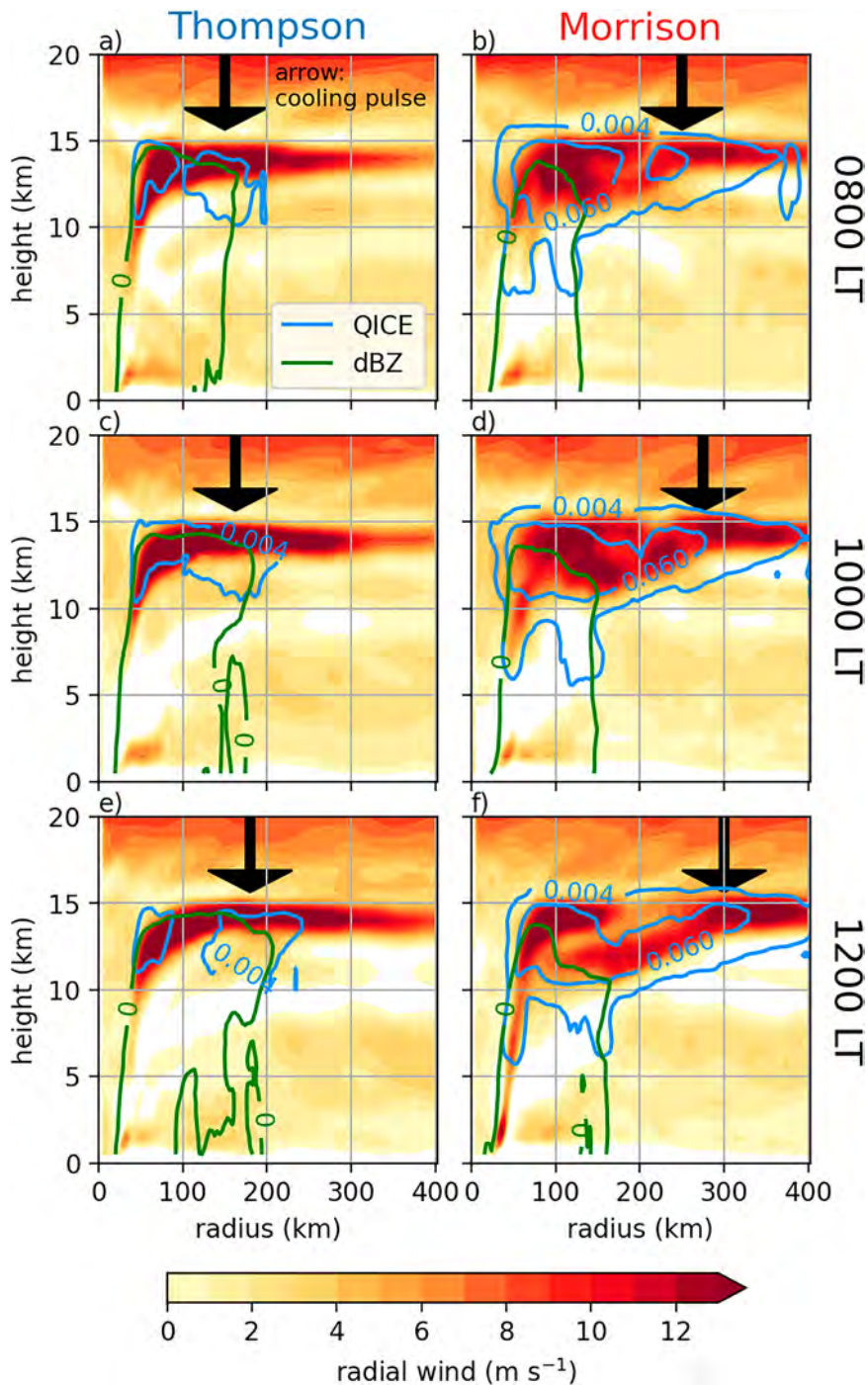


FIG. 12. Vertical cross sections of azimuthally averaged radial wind (shaded; m s^{-1}), QICE (blue; g kg^{-1}), and reflectivity (green; dBZ) west of the storm center at (a) 0800, (b) 1000, and (c) 1200 LT 1 Sep for (a),(c),(e) Thompson CTRL and (b),(d),(f) Morrison CTRL. Black arrows indicate the position of the CP at each time step following Figs. 4b and 4c.

increase seems largely coincidental and was likely due to smaller, unorganized cells that occurred at 300 km.

The propagation and origin of each CP can be illustrated by azimuthally averaged vertical cross sections of reflectivity,

radial outflow, and cloud ice mixing ratio (QICE) at 0800, 1000, and 1200 LT (Fig. 12). The 0600 LT cross sections are excluded because the CP signatures were quite weak at the time. Variations in QICE amounts are generally responsible

for changes in IRBT; [Dunion et al. \(2019\)](#) showed outward propagations of QICE associated with simulated CPs in a hurricane nature run. Similarly, Thompson CTRL's CP (black arrows in [Figs. 12a,c,e](#)) was collocated with enhanced QICE (blue contours in [Figs. 12a,c,e](#)). The QICE maximum slowly propagated radially outward with the rainband shown in [Figs. 9a, 9c, and 9e](#), whose outward edge is marked by a green 0-dBZ contour, such that both were positioned near 175 km by 1200 LT ([Fig. 12e](#)). This QICE maximum largely was situated between 10 and 14 km, below the strongest radial winds of the upper-level outflow.

As anticipated through its larger cloud shield ([Fig. 5e](#)), Morrison CTRL featured greater amounts of QICE at all timesteps; its CP was tied to a QICE maximum, unassociated with a rainband ([Figs. 12b,d,f](#)). Instead, Morrison CTRL's CP aligned well with relatively greater magnitudes of positive (outward) radial wind. These different QICE tendencies suggest that the QICE associated with the Morrison CTRL CP was advected by outflow at upper levels, while the QICE associated with the Thompson CTRL CP was generated by deep convection within the rainband. It is noteworthy that the Morrison CTRL outflow channel split into inner and outer layers within 100 km by 1200 LT ([Fig. 12f](#)). The split outflow was collocated with the outward propagation of large reflectivity bands from the eyewall ([Figs. 9b,d](#)), potentially in the form of vortex Rossby waves (VRWs; [Corbosiero et al. 2006](#)), which invigorated ascent and generated a secondary outflow channel (not shown). The hypothesized VRWs occurred after the CP propagated outward to almost 300 km and, thus, should not be considered a factor in its evolution.

Although diurnal pulses were originally detected from observed IRBT fields, we argue that IRBT alone is inadequate for tracking simulated diurnal pulses because it is substantially modulated by variations in MP schemes that may not be important to the pulses themselves, their generation mechanism(s), and consequences regarding hazardous weather and storm behavior. IRBT fluctuations are mere symptoms of other underlying processes that seem to be related to rainbands (convectively coupled CPs) or upper-level outflow (canopy-restricted CPs).

4. Discussion and conclusions

Diurnal pulses, both CPs and WPs, are common in TCs worldwide ([Dunion et al. 2014](#); [Ditchek et al. 2019b](#); [Zhang and Xu 2022](#)). The current study shows that CPs are also prevalent in simulations of Hurricane Dorian (2019) that use either Thompson or Morrison MP schemes. Among these simulations, however, there are substantial distinctions regarding CP timing, intensity, and structure, suggesting different driving mechanisms behind diurnal pulses. To summarize and discuss findings, the research questions posed in the introduction are revisited.

a. How does choice of MP scheme impact CP characteristics? How do simulated CPs compare to the observed?

Both Thompson CTRL and Morrison CTRL produced CPs on 1–2 September west of the TC center. The Thompson CPs were convectively coupled, occurring in tandem with precipitation pulses (PPs) out to 300 and 400 km on 1 and 2 September,

respectively. The Morrison CPs featured no associated rainband; rather, they were restricted to the cirrus canopy. The Morrison CPs also propagated radially farther, out to 600 km. The CP radial extent and cloud shield size of Thompson CTRL better matched the 1 September observations. The Morrison CTRL cloud shield was much larger because the Morrison MP tends to feature enhanced concentrations of free-floating, and thus easily advected, cloud ice in the cirrus canopy. Clearly, the MP scheme itself has a substantial influence on IRBT due to different approximations that are unrelated to pulses or the TCDC in general. As a result, we argue that using IRBT alone to detect diurnal pulses is suboptimal, particularly within simulations, and that more emphasis should be placed on reflectivity and rain rate.

b. What is the origin of CPs, and what causes their outward propagation?

Cooler IRBT was correlated with enhanced free-floating cloud ice between 10- and 15-km height. The source of propagating cloud ice differed between Thompson and Morrison MP, however. For Thompson, whereby the CP was convectively coupled, cloud ice was created in situ above an outward propagating rainband. [Ditchek et al. \(2020\)](#) showed that convectively coupled CPs become reinvigorated within more unstable environments as they exit the inner core, but future work must determine why this process often occurs off-the-clock. For Morrison, whereby the CP was restricted to the cirrus canopy, enhanced cloud ice propagated outward in the upper-level outflow layer from the TC inner core, apart from any rainband. Vertical cross sections suggest that this enhanced cloud ice sprouted from temporarily more robust eyewall deep convection that appears to be tied to the diurnal cycle, but future work should explore this mechanism further.

c. Discussion

By classifying CPs as either canopy-restricted or convectively coupled, our results show where previous hypotheses regarding diurnal pulse generation may or may not be true. Gravity waves, for instance, are theorized to induce pulses, namely, because 1) diurnal gravity waves propagate radially outward at similar speeds to observed and simulated diurnal pulses ([Dunion et al. 2014](#); [Navarro and Hakim 2016](#); [Ditchek et al. 2019a,b](#); [Ruppert and O'Neill 2019](#)) and 2) simulated CPs and WPs are associated with upper-level updrafts and downdrafts, respectively ([Dunion et al. 2019](#); [Ruppert and O'Neill 2019](#)). Interestingly, idealized simulations suggest that the radiation of diurnal gravity waves is restricted to the upper troposphere (e.g., the cirrus canopy) and outer radii (>500 km) due to the relatively large inertial stability in the TC near core ([O'Neill et al. 2017](#); [Evans and Nolan 2019](#)). Thus, gravity waves are more likely driving canopy-restricted CPs rather than convectively coupled CPs, which are tied to the lower troposphere and occur relatively closer to the storm center ([Zhang and Xu 2022](#)). Instead, convectively coupled CPs seem to originate from inner rainbands, which, as shown by [Ditchek et al. \(2020\)](#), often then propagate outward into convectively favorable environments and reinvigorate. How

each of these CP types are precisely generated with respect to the diurnal cycle of solar radiation is still unclear, however. Future work will address this issue to enhance overall pulse predictability and also to explain why pulses occur off-the-clock.

While IRBT can be useful for identifying TC trends when other observations are unavailable, pulses must be classified based on other variables that more directly illustrate underlying processes rather than their symptoms. The use of other fields is especially crucial when diagnosing pulses in simulations, where IRBT is substantially modified by MP scheme. Fields such as reflectivity, rain rate, and other thermodynamic and dynamic variables are much more useful in determining how diurnal pulses impact storm intensity, structure, and hazardous weather (Dunion et al. 2019; Ditchek et al. 2020), which is why interest in diurnal pulses originally began (Dunion et al. 2014).

Acknowledgments. The authors thank the editor and three anonymous reviewers for their effort to improve this manuscript. This research was funded by the University at Albany Carson Carr Graduate Fellowship, NSF Grant AGS1636799, and NOAA Collaborative Science, Technology, and Applied Research (CSTAR) Program Grant NA19NWS4680006.

Data availability statement. The Best Track Dataset (HURDAT2; Landsea and Franklin 2013) is publicly available at <https://www.nhc.noaa.gov/data/>. GridSat-B1 data (Knapp et al. 2011) are publicly available at <https://www.ncdc.noaa.gov/gridsat/>. GFS simulations used to force WRF simulations are publicly available at <https://www.ncei.noaa.gov/products/weather-climate-models/global-forecast>. WRF simulations were created and are stored on NCAR's Cheyenne supercomputer (Computational and Information Systems Laboratory 2017) and are available upon request.

REFERENCES

- Bao, J.-W., S. A. Michelson, and E. D. Grell, 2019: Microphysical process comparison of three microphysics parameterization schemes in the WRF Model for an idealized squall-line case study. *Mon. Wea. Rev.*, **147**, 3093–3120, <https://doi.org/10.1175/MWR-D-18-0249.1>.
- Bu, Y. P., R. G. Fovell, and K. L. Corbosiero, 2014: Influence of cloud–radiative forcing on tropical cyclone structure. *J. Atmos. Sci.*, **71**, 1644–1662, <https://doi.org/10.1175/JAS-D-13-0265.1>.
- Computational and Information Systems Laboratory, 2017: Cheyenne: SGI ICE XA Cluster. UCAR/NCAR, accessed 1 March 2023, <https://doi.org/10.5065/D6RX99HX>.
- Corbosiero, K. L., J. Molinari, A. R. Aiyyer, and M. L. Black, 2006: The structure and evolution of Hurricane Elena (1985). Part II: Convective asymmetries and evidence for vortex Rossby waves. *Mon. Wea. Rev.*, **134**, 3073–3091, <https://doi.org/10.1175/MWR3250.1>.
- Ditchek, S. D., K. L. Corbosiero, R. G. Fovell, and J. Molinari, 2019a: Electrically active tropical cyclone diurnal pulses in the Atlantic basin. *Mon. Wea. Rev.*, **147**, 3595–3607, <https://doi.org/10.1175/MWR-D-19-0129.1>.
- , J. Molinari, K. L. Corbosiero, and R. G. Fovell, 2019b: An objective climatology of tropical cyclone diurnal pulses in the Atlantic basin. *Mon. Wea. Rev.*, **147**, 591–605, <https://doi.org/10.1175/MWR-D-18-0368.1>.
- , K. L. Corbosiero, R. G. Fovell, and J. Molinari, 2020: Electrically active diurnal pulses in Hurricane Harvey (2017). *Mon. Wea. Rev.*, **148**, 2283–2305, <https://doi.org/10.1175/MWR-D-20-0022.1>.
- Dunion, J. P., C. D. Thorncroft, and C. S. Velden, 2014: The tropical cyclone diurnal cycle of mature hurricanes. *Mon. Wea. Rev.*, **142**, 3900–3919, <https://doi.org/10.1175/MWR-D-13-00191.1>.
- , —, and D. S. Nolan, 2019: Tropical cyclone diurnal cycle signals in a hurricane nature run. *Mon. Wea. Rev.*, **147**, 363–388, <https://doi.org/10.1175/MWR-D-18-0130.1>.
- Duran, E. L., E. B. Berndt, and P. Duran, 2021: Observation of the tropical cyclone diurnal cycle using hyperspectral infrared satellite sounding retrievals. *Mon. Wea. Rev.*, **149**, 3671–3690, <https://doi.org/10.1175/MWR-D-20-0415.1>.
- Evans, R. C., and D. S. Nolan, 2019: Balanced and radiating wave responses to tropical heating in tropical cyclone-like vortices using a linear nonhydrostatic model. *J. Atmos. Sci.*, **76**, 2575–2597, <https://doi.org/10.1175/JAS-D-18-0361.1>.
- Fovell, R. G., K. L. Corbosiero, A. Seifert, and K.-N. Liou, 2010: Impact of cloud-radiative processes on hurricane track. *Geophys. Res. Lett.*, **37**, L07808, <https://doi.org/10.1029/2010GL042691>.
- Ge, X., Y. Ma, S. Zhou, and T. Li, 2014: Impacts of the diurnal cycle of radiation on tropical cyclone intensification and structure. *Adv. Atmos. Sci.*, **31**, 1377–1385, <https://doi.org/10.1007/s00376-014-4060-0>.
- Hazelton, A., G. J. Alaka Jr., M. S. Fischer, R. Torn, and S. Gopalakrishnan, 2023: Factors influencing the track of Hurricane Dorian (2019) in the West Atlantic: Analysis of a HAFS ensemble. *Mon. Wea. Rev.*, **151**, 175–192, <https://doi.org/10.1175/MWR-D-22-0112.1>.
- Iacono, M. J., J. S. Delamere, E. J. Mlawer, M. W. Shephard, S. A. Clough, and W. D. Collins, 2008: Radiative forcing by long-lived greenhouse gases: Calculations with the AER radiative transfer models. *J. Geophys. Res.*, **113**, D13103, <https://doi.org/10.1029/2008JD009944>.
- Kain, J. S., 2004: The Kain–Fritsch convective parameterization: An update. *J. Appl. Meteor.*, **43**, 170–181, [https://doi.org/10.1175/1520-0450\(2004\)043<0170:TKCPAU>2.0.CO;2](https://doi.org/10.1175/1520-0450(2004)043<0170:TKCPAU>2.0.CO;2).
- Knapp, J. A., C. J. Slocum, and K. D. Musgrave, 2019: Quantification and exploration of diurnal oscillations in tropical cyclones. *Mon. Wea. Rev.*, **147**, 2105–2121, <https://doi.org/10.1175/MWR-D-18-0379.1>.
- Knapp, K. R., and Coauthors, 2011: Globally gridded satellite observations for climate studies. *Bull. Amer. Meteor. Soc.*, **92**, 893–907, <https://doi.org/10.1175/2011BAMS3039.1>.
- Landsea, C. W., and J. L. Franklin, 2013: Atlantic hurricane database uncertainty and presentation of a new database format. *Mon. Wea. Rev.*, **141**, 3576–3592, <https://doi.org/10.1175/MWR-D-12-00254.1>.
- Lee, J.-D., C.-C. Wu, and K. Ito, 2020: Diurnal variation of the convective area and eye size associated with the rapid intensification of tropical cyclones. *Mon. Wea. Rev.*, **148**, 4061–4082, <https://doi.org/10.1175/MWR-D-19-0345.1>.
- Melhauser, C., and F. Zhang, 2014: Diurnal radiation cycle impact on the pregenesis environment of Hurricane Karl (2010). *J. Atmos. Sci.*, **71**, 1241–1259, <https://doi.org/10.1175/JAS-D-13-0116.1>.
- Morrison, H., G. Thompson, and V. Tatarskii, 2009: Impact of cloud microphysics on the development of trailing stratiform precipitation in a simulated squall line: Comparison of one- and two-moment schemes. *Mon. Wea. Rev.*, **137**, 991–1007, <https://doi.org/10.1175/2008MWR2556.1>.

- Nakanishi, M., and H. Niino, 2009: Development of an improved turbulence closure model for the atmospheric boundary layer. *J. Meteor. Soc. Japan*, **87**, 895–912, <https://doi.org/10.2151/jmsj.87.895>.
- Navarro, E. L., and G. J. Hakim, 2016: Idealized numerical modeling of the diurnal cycle of tropical cyclones. *J. Atmos. Sci.*, **73**, 4189–4201, <https://doi.org/10.1175/JAS-D-15-0349.1>.
- Nguyen, L. T., J. Molinari, and D. Thomas, 2014: Evaluation of tropical cyclone center identification methods in numerical models. *Mon. Wea. Rev.*, **142**, 4326–4339, <https://doi.org/10.1175/MWR-D-14-00044.1>.
- Niu, G.-Y., and Coauthors, 2011: The community Noah land surface model with multiparameterization options (Noah-MP): 1. Model description and evaluation with local-scale measurements. *J. Geophys. Res.*, **116**, D12109, <https://doi.org/10.1029/2010JD015139>.
- O'Neill, M. E., D. Perez-Betancourt, and A. A. Wing, 2017: Accessible environments for diurnal-period waves in simulated tropical cyclones. *J. Atmos. Sci.*, **74**, 2489–2502, <https://doi.org/10.1175/JAS-D-16-0294.1>.
- Petty, G. W., 2006: *A First Course in Atmospheric Radiation*. Sundog Publishing, 459 pp.
- Ruppert, J. H., Jr., and M. E. O'Neill, 2019: Diurnal cloud and circulation changes in simulated tropical cyclones. *Geophys. Res. Lett.*, **46**, 502–511, <https://doi.org/10.1029/2018GL081302>.
- Skamarock, W. C., and Coauthors, 2019: A description of the Advanced Research WRF Model version 4. NCAR Tech. Note NCAR/TN-556+STR, 145 pp., <https://doi.org/10.5065/1dfh-6p97>.
- Tang, X., and F. Zhang, 2016: Impacts of the diurnal radiation cycle on the formation, intensity, and structure of Hurricane Edouard (2014). *J. Atmos. Sci.*, **73**, 2871–2892, <https://doi.org/10.1175/JAS-D-15-0283.1>.
- Thompson, G., P. R. Field, R. M. Rasmussen, and W. D. Hall, 2008: Explicit forecasts of winter precipitation using an improved bulk microphysics scheme. Part II: Implementation of a new snow parameterization. *Mon. Wea. Rev.*, **136**, 5095–5115, <https://doi.org/10.1175/2008MWR2387.1>.
- Trabing, B. C., and M. M. Bell, 2021: Observations of diurnal variability under the cirrus canopy of Typhoon Kong-rey (2018). *Mon. Wea. Rev.*, **149**, 2945–2964, <https://doi.org/10.1175/MWR-D-20-0327.1>.
- Zhang, J. A., J. P. Dunion, and D. S. Nolan, 2020: In situ observations of the diurnal variation in the boundary layer of mature hurricanes. *Geophys. Res. Lett.*, **47**, 2019GL086206, <https://doi.org/10.1029/2019GL086206>.
- Zhang, X., and W. Xu, 2022: Is there an outward propagating diurnal signal in the precipitation of tropical cyclones? *Geophys. Res. Lett.*, **49**, e2021GL097166, <https://doi.org/10.1029/2021GL097166>.